Title	Differential surface representation for myocardial deformation
Author(s)	Chiang, Patricia; Cai, Yiyu; Mak, K. H.; Zheng, Jianmin
Citation	Chiang, P., Cai, Y., Mak, K. H., & Zheng, J. (2014). Differential surface representation for myocardial deformation. Experimental and clinical cardiology, 20(8), 2720-2747.
Date	2014
URL	http://hdl.handle.net/10220/25294
Rights	© 2014 The Author(s) (Published by Cardiology Academic Press). This paper was published in Experimental and Clinical Cardiology and is made available as an electronic reprint (preprint) with permission of The Author(s) (Published by Cardiology Academic Press). The paper can be found at the following URL: [http://cardiologyacademicpress.com/soap/pdf/delme_1863_53e54be9bfdd44.61117913.pdf]. One print or electronic copy may be made for personal use only. Systematic or multiple reproduction, distribution to multiple locations via electronic or other means, duplication of any material in this paper for a fee or for commercial purposes, or modification of the content of the paper is prohibited and is subject to penalties under law.

EXPERIMENTAL & CLINICAL
Cardiology

EXPERIMENTAL & CLINICAL CARDIOLOGY

Volume 20, Issue 8, 2014

Title: "ï€ Differential Surface Representation for Myocardial Deformation"

Authors: Jm Zheng, Y Cai and Patricia Chiang

How to reference: ? Differential Surface Representation for Myocardial Deformation/Jm Zheng, Y Cai and Patricia Chiang/Exp Clin Cardiol Vol 20 Issue8 pages 2720-2747 / 2014

Differential Surface Representation for Myocardial Deformation

Patricia Chiang[1], YY Cai[1,2,*], KH Mak[3], and JM Zheng[4]

[1]School of Mechanical & Aerospace Engineering, Nanyang Technological University,

50 Nanyang Avenue, Singapore 639798

[2]Institute for Media Innovation, Nanyang Technological University,

50 Nanyang Drive, Singapore 637553

[3]Mak Heart Clinic, Gleneagles Medical Center, 6 Napier Road, Singapore 258499

[4]School of Computer Engineering, Nanyang Technological University,

50 Nanyang Avenue, Singapore 639798

[*]Corresponding author, Tel/Fax: 65-67905777, Email: myycai@ntu.edu.sg

Abstract: In this paper, we propose a differential surface representation for spatio-temporal tracking of myocardial deformation of the left ventricle (LV) from tagged MRI scans. The 4D tracking problem is formulated as a linear optimization function that minimizes the changes in local differential characteristics and differences between projected and tracked in-plane displacements. Compared to existing arts that fit displacements to model in separate components, the proposed method resolves the apparent motion by global and local mesh deformation considerations. The method has successfully been applied to reconstruct the motion for the LV for a set of tagged MRI

scans to produce a 0.2 local linear shortening, 10.3° twist, 25% radial compression and 16% longitudinal compression.

Key Words: *Differential Surface Representation, spatio-temporal tracking, free form deformation, myocardial deformation, mesh,* Motion Reconstruction, *tagged MRI (tMRI)*

1. Introduction

A percutaneous intra-cardiac intervention allows for the diagnosis of ischemic regions in the heart and the therapeutic treatment to restore myocardial function through stem cell injection in the same surgical setting. Despite its potential, the procedure remains complex and interventional cardiologists require intensive training to navigate the catheter in the heart lumen and precisely administer the injection. The development of a VR simulator will fulfill surgical training needs and improve the efficacy of the procedure. Our recent interest includes the design and development of VR simulator for intra-cardiac simulation [28], the modeling of the catheter-heart interaction [29], the progressive reconstruction for electromechanical mapping [30], and heart motion extraction from tagged MRI (tMRI) data [31]. A dynamic heart model is critical to simulate the realistic interaction between the catheter and heart wall in a VR simulator for intra-cardiac intervention. The modeling of whole heart [1] comprises of construction of heart geometry, inclusion of special conduction network and anisotropic myofibers and electrophysiological considerations. Traditional modeling simulates the heart wall contraction from electrocardiogram using electromechanical models at multi-scale level [2][3][4] that incorporate Purkinje network and myofiber structure. However, these

complex models require validation and are not easily customized. Alternatively, patient specific motion data can be extracted directly from non-invasive imaging techniques like cardiac tMRI for reconstructing dynamic heart model. The spatio-temporal tracking of myocardial deformation from tMRI can provide LV functional measures such as strain and torsion.

tMRI applies temporary non-invasive tagging pattern to the myocardium at end diastole. The tagging pattern comes from a periodic planar RF variation that is orthogonal to the imaging plane. Tag planes are formed by points having phase of π in the volume. As the heart contracts, the tag plane deforms with the motion of myocardium and the tag pattern is captured in an imaging slice for a time series. The imaging plane is fixed for the capture but the motion of myocardium may not be parallel to the imaging plane. Hence, planar motion tracking on a slice captures only apparent motion and not through plane motion.

Generally, the spatial-temporal tracking of myocardial deformation recovers the 3D motion of the heart by integrating different sets of apparent motion into 4D domain. Spatial refers to 3D space and temporal refers to frames in the cardiac cycle. The reconstructed dynamic heart model provides useful myocardial functional measurements. The framework includes setting up of an appropriate model, tracking of component motions and modeling of 4D myocardial deformation. The models described in existing arts are of a varied representation including volume, surface, surface-bounded volume or point set having spatial or temporal continuity. Volumetric model requires transmural input while continuous model may not be able to describe motion fully. The input data to such algorithms may be dense or sparse for example tag points on tag lines, extracted tag

lines, intersection of tag lines and contours. One important consideration of the algorithms is the conversion of the apparent 2D motion to 3D motion through constraints, integration or component additions. The results are typically evaluated by motion profile on in-vivo MRI dataset and their error performance on simulated images with kinematics model like Arts *et al.* [5], Waks *et al.* [6] and Waldmann *et al.* [7].

In early work by O'Dell *et al.* [8], a truncated power series is used to fit the displacement data from three orthogonal sets of tagged 1D MRI. The method represents 3D deformation in a small number of parameters but may not be sufficient to represent local deformations. Using a physics-based approach, Park *et al.* [9] model the LV deformation with Lagrangian dynamics and finite element method (FEM). Each volumetric prism is deformed with 3D nodal displacements from tag points and LV boundaries. The LV is further described by a deformable model with parametric functions that captures global deformations like twisting and radial and longitudinal contraction intuitively for clinical evaluation. Haber *et al.* [10] extend the work of Park *et al.* to the right ventricle (RV). However, volumetric finite elements are vulnerable to degeneration and may require tedious remeshing for optimal representation. Using similar Lagrangian dynamics, Wang *et al.* [11] propose a meshless model where global deformation is computed by integrating each particle, grouped in phyxel with kernel function, over the myocardium. Local tag displacements and moving least squares mesh strains are defined as external and internal forces in the Lagrange equation. The method requires large iterations and assumes isotropic characteristics.

From the perspective of geometry, the 3D myocardium deformation relates to a 4D fitting problem of B-Spline and Non-Uniform Rational B-Spline (NURBS) models. Luo *et al.*

[12] improvise the work of Park *et al.* by representing the deformable model in terms of 4D B-Spline. The backward displacements are modeled with a B-Spline solid where each component displacement is fitted independently with a fast hierarchical algorithm. Motion parameters are estimated with 3D B-Splines in time sequence by minimizing the sum of difference between estimated and true motion. Ozturk *et al.* [13] model backward displacements with 2D Splines by performing a first fitting of in-plane displacements from tagged points and a second fitting of out-of-plane interpolated displacements from orthogonal slices. The forward spatial-temporal displacements are then modeled by a 4D B-Spline tensor. Similarly, Huang *et al.* [14] models the myocardial deformation with a 4D B-Spline, fitting each knot plane to each tagged plane by minimizing the Chamfer distance potential. The planes are combined to give a B-Spline solid for each time instant and the solids are combined to give the 4D B-Spline. The B-Splines provide a continuous representation but the grid-like control is not optimally distributed for an enclosure with relatively large lumen. To match the shape of the LV better, Li *et al.* [15] defines the B-Spline deformation model in prolate spheroid coordinates. Tustison *et al.* [16] extend the B-Spline to model biventricular deformations with a cylindrical parameterized Cartesian NURBS but the set of control nodes is sparse.

Rather than translating the apparent 2D motion to independent constraints in 3D deformation, Kerwin *et al.* [17] tracks the true motion of the intersections between orthogonal set of tag planes within the segmented myocardium. The deformation of each tag plane is modeled with a thin plate Spline and the intersections are determined by an alternating projection algorithm. This algorithm however requires much iteration for convergence. Pan *et al.* [18] propose a 3D HARmonic Phase imaging (HARP) analysis on

2D tagged SA and 1D tagged LA MRI scans. A half elliptical spheroid is initialized with 3D phase values and deformed with in-plane motion. The deformation is subsequently corrected through iterations with 2D motion tracking to satisfy the invariant phase property. The mesh however comprises only 72 quad elements and the convergence of the iterations needs to be further accessed. Instead of working on an algorithm to overcome the limitation of through-plane motion, Sampath *et al.* [19] present a modified imaging technique SF-CSPAMM (Slice Following Complementary SPAtial Modulation of Magnetization) technique that images a thick slice to cover the through-plane motion of the thin tagged slice. The true motion is derived directly by tracking the material points on intersections between orthogonal SA and LA slices. However this method is not available on commercial MRI scanners.

Our proposal models the myocardial deformation with a differential surface representation, which is more suited for the assessing wall surface contractile properties for intra-cardiac intervention. Rather than working on separate component displacement constraints in B-Splines or NURBS, we integrate the apparent motion into an optimization function that minimizes the local differential characteristics and the differences between the projected and tracked in-plane displacements. This optimization is reduced to a sparse linear system that can be easily solved with a linear algebraic package. The discrete nature of the mesh has a lower complexity and a higher flexibility to representing deformation compared to continuous models or FEM models. Although our method have neither direct representation of clinical intuitive parameters nor strain analysis, the clinical parameters can be analyzed at a post-processing stage. The paper focuses on the reconstruction of the LV to generate a patient specific dynamic heart

model for simulation of intra-cardiac intervention. However, the method is applicable to the RV.

2. Spatio-Temporal Tracking of Myocardial Deformation with Differential Surface Representation

2.1 Overview

The overview of the proposed 3D motion reconstruction from patient specific tMRI is described herein. From the cardiac tMRI DICOM files provided by a MRI scanner, the images are cropped and scaled for motion tracking. Some material points lining the ventricular lumen are marked on the initial frame of slices in SA and LA planes. The material markers are tracked with the HARP method throughout the cardiac cycle. HARP is a dense motion tracking algorithm based on the invariant phase and these markers represent only a small subset of the tracking results. The 3D positions of the markers are found using respective slice orientation and origin. Cardiac landmarks of aortic valve, mitral valve and apex are identified in the tMRI scans for mesh alignment. A prolate spheroid mesh is first fitted to the initial frame and is subsequently deformed with the planar tracked material points to reconstruct the 3D motion. The reconstructed motion is further integrated into the heart model.

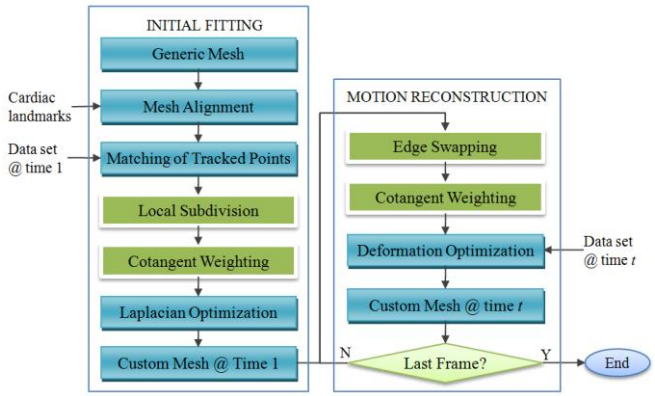

Fig. 1: Spatio-temporal tracking of myocardial deformation

2.2 Initial Fitting

Referring to Fig. 1, the initial geometry of the LV is first achieved by deforming a generic mesh to fit a set of material points at time 1. The generic mesh is globally transformed through rotation, scaling and translation with the cardiac landmarks. A prolate spheroid model is used in our work to approximate the shape of LV where the spheroid co-ordinates are translated to align the co-ordinate origin to 2/3 the distance from the apex to base. Then, the set of material points is paired to the mesh vertices using the smallest Euclidean distance criterion. The mesh is locally subdivided at the paired vertex for a better fit. The area of subdivision is defined in the neighborhood of the paired vertex and the mesh is re-triangulated to remove cracks caused by a difference in subdivision depth. A simple adaptive subdivision [20] of depth 1 may be used. Alternatively, an incremental adaptive loop subdivision [21] scheme of equal or higher depth may be employed where the area of subdivision is extended into immediate triangles to allow a gradual change in subdivision depth. Fig. 2 shows the new vertices and edges generated for the edge-centered simple adaptive subdivision and triangle-centered incremental adaptive

subdivision scheme. The co-tangent weights [22] of the mesh are computed for a subsequent Laplacian optimization [23].

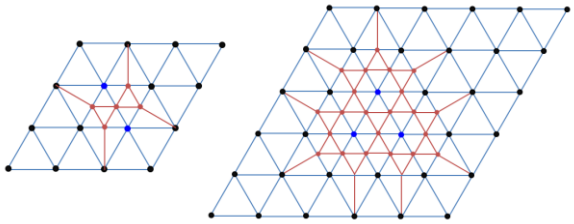

(a) (b)

Fig. 2: (a) Simple adaptive subdivision centered on edge (blue); (b) Incremental adaptive subdivision centered on triangle (blue); New vertices and edges are generated (red).

Let $p_i(t)$ be the *i*-th vertex in a set of mesh vertices **P** at time t and $s_j(t)$ be the *j*-th material point in a dataset **S** from the planar tracked motion at time t; $p_{idx(j)}(t)$ corresponds to the mesh vertex that is paired with the *j*-th material point; The Laplacian vector at vertex p_i is defined as $L(p_i) = \sum_{k \in N(i)} \omega_{ik}(p_i - p_k)$ where ω_{ik} refers to the co-tangent weight corresponding to the edge e_{ik}, formed by vertex p_i and another vertex p_k in its neighborhood; Co-tangent weight is described by $\omega_{ik} = \frac{1}{2}(\cot\alpha_{ik} + \cot\beta_{ik})$ where α_{ik} and β_{ik} are opposite angles of e_{ik}. T_i is the local transformation matrix at vertex p_i and can be decomposed into a scaling matrix S_i and a rotation matrix R_i such that $T_i = S_i R_i$.We write the Laplacian optimization problem as:

$$F_1(\mathbf{P},t) = \sum_{p_i \in \mathbf{P}} \| L(p_i(t)) - T_i(t) L(p_i(t-1)) \|^2 + \alpha \sum_{s_j \in \mathbf{S}} \| p_{idx(j)}(t) - s_j(t) \|^2 \quad (1)$$

where α weighs between the smoothing and fidelity terms. The smoothing term ensures that the initial fitting preserves the local Laplacian characteristics of the surface for describing the mean surface curvature, while the fidelity term constraints the deformation

for the input set of material points to match the set of paired vertices. The custom mesh at $t=1$ is a solution to the minimization of $F(\mathbf{P},t)$. By setting $T_i = I$ (identity matrix), we first derive a naïve solution of $\mathbf{P}$ at time t. The rotation matrix can be computed from the eigenvectors of the covariance matrix between edges from the naïve solution at time t, and edges of the mesh at time $t-1$ [24]. Having found the rotation matrix, the scaling matrix can be derived by minimizing the absolute difference between edges from the naïve solution at time t, and the locally transformed edges of the mesh at time $t-1$. Fixing the transformation matrix, we solve the minimization of (1) with linear least squares for the initial geometry of the LV.

2.3 Motion Reconstruction

After the initial geometry, the mesh is deformed for spatio-temporal tracking of material points. The correlation between the material point and mesh vertex is maintained as the material points from myocardial tissue are tracked from the initial to the end frame of a cardiac cycle with the HARP method. An edge swapping process [20] is first performed with a mean curvature criterion to improve the mesh geometry from the previous deformation. Let e_{ij} be an edge formed by the *i*-th vertex and the *j*-th vertex that is adjacent to two triangles T_{ijk} and T_{hij} in Fig. 3. If the swapping configuration satisfy a criterion, e_{ij} will be swapped with new edge e_{hk} by disconnecting the *i*-th and *j*-th vertices and connecting the *h*-th and *k*-th vertices. The criterion is described by a smaller local curvature near e_{hk} than e_{ij} and that e_{hk} is locally Delaunay. The local curvatures are computed by the sum of inverse cosine angle between the normals of the triangles in the

neighborhood of the edge and its swapped configuration. An edge e_{ij} is locally Delaunay if its cotangent weight is non-negative. The edge swapping process is applied to every edge of the mesh for several iterations. Alternatively, a minimum area criterion may be used for edge swapping. The cotangent weights are updated for the new positions from the previous deformation and new connectivity of the vertices from the edge swapping.

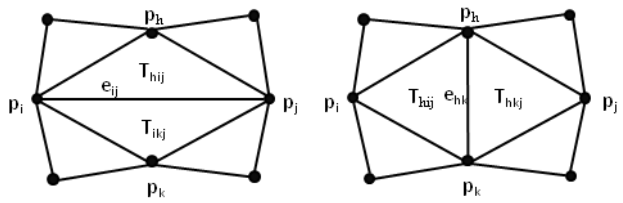

Fig. 3: Edge swapping configurations

As the planar tracking provides only the apparent motion of the material points, we have to modify the fidelity term in (1). Here, we present a new deformation optimization function that integrates the apparent motion from orthogonal planes with differential surface characteristics. Let $\mathbf{S}_1$, $\mathbf{S}_2$ and $\mathbf{S}_3$ be exclusive subsets of dataset $\mathbf{S}$ from different imaging planes in SA and LA slices where $\hat{n}_1$, $\hat{u}_2$ and $\hat{u}_3$ are respective imaging plane unit normal and tagging plane unit normals. In our work, we have three orthogonal sets of images, a 2D tagging grid on the SA slices and 1D tagging lines on both the horizontal LA and vertical LA slices. The deformation of the mesh at time t is estimated by minimizing the following optimization function:

$$
\begin{aligned}
F_2(\mathbf{P},t) = \lambda_1 \sum_{p_i \in \mathbf{P}(t)} \| L(p_i(t)) - T(t)L(p_i(t-1)) \|^2 \\
+ \lambda_2 \sum_{s_j \in \mathbf{S_1}(t)} \left\| (\hat{n}_1 \hat{n}_1^{\,T} - I)(p_{idx(j)}(t) - s_j(t)) \right\|^2 \\
+ \lambda_3 \sum_{s_j \in \mathbf{S_2}(t)} \left\| \hat{u}_2 \hat{u}_2^{\,T} (p_{idx(j)}(t) - s_j(t)) \right\|^2 \\
+ \lambda_4 \sum_{s_j \in \mathbf{S_3}(t)} \left\| \hat{u}_3 \hat{u}_3^{\,T} (p_{idx(j)}(t) - s_j(t)) \right\|^2
\end{aligned}
\tag{2}
$$

where λ_1, λ_2, λ_3 and λ_4 are weights to balance the smoothing and fidelity terms. The first term preserves the local surface curvature by minimizing the square sum of Laplacian from the deformation at time $t-1$. The remaining terms integrate the motion data by minimizing the sum of differences between apparently displaced material points and the projections of their paired mesh vertices for various imaging planes. The second term is used to fit motion data from an image plane with a 2D tagging grid. A mesh vertex $p_{idx(j)}$ that is paired to a material point s_j, is projected onto the image plane to give $p'_{idx(j)} = (I - \hat{n}_1 \hat{n}_1^{\,T})(p_{idx(j)} - s_j) + s_j$. Both the third and fourth terms are used for fitting motion data from image planes with 1D tags. A paired mesh vertex p_j is projected to the tagging plane normal to give $p'_{idx(j)} = \hat{u}_2 \hat{u}_2^{\,T}(p_{idx(j)} - s_j) + s_j$. In our work, we use the SA plane data for plane projection and the LA planes for line projections. This formulation can be applied to combine motion data from imaging planes that are not orthogonal to each other. By using projection data in a global optimization, we eliminate the need to model separately for displacements in each component. The solution to (2) generates a custom mesh approximating the surface deformation of the LV at each time t. We set $\lambda_1 = 1$, $\lambda_2 = 0.0317$ and $\lambda_3 = \lambda_4 = 0.0156$ heuristically. The weight λ_2 should be larger than weights λ_3 and λ_4, since the second term represents two displacement components while

the third and fourth terms represent only one component. A larger λ_1 will provide a solution of a closer fit to the initial geometry of the LV while larger λ_2, λ_3 and λ_4 allows for larger deformation of the reconstructed LV. Visible distortion might result if the latter weights are large.

2.4 Integration

The simulator for intra-cardiac intervention comprises of a high resolution tetrahedron heart model and a catheter model to describe the interaction between catheter and heart surface. The catheter is modeled as an array of (*N+1*) nodes $\{q_i\}_0^N$ joined by rigid segments. The catheter insertion at the aortic orifice lies between the *I*-th and (*I+1*)-th catheter nodes while the catheter tip is represented by the *N*-th catheter node. The tetrahedron heart model is deformed according to the reconstructed motion of the LV via free form deformation (FFD) to generate a patient specific dynamic heart model for the simulator. Let $h(x,y,z,t)$ represent a point in the Cartesian space of the heart model **H** and $h(u,v,w,t)$ is in normalized local co-ordinates. We estimate the deformation of the heart model $\tilde{h}(u,v,w,t)$ through a trivariate tensor product Bernstein polynomial function:

$$\tilde{h}(u,v,w,t)=\sum_{k=0}^{l}\sum_{j=0}^{m}\sum_{i=0}^{n}P_{ijk}(t)B_i^n(u)B_j^m(v)B_k^l(w) \qquad (3)$$

where $B_i^n(u)$, $B_j^m(v)$ and $B_k^l(w)$ are the Bernstein polynomials. The control points $P_{ijk}(t)$ for the deformation at time t can be found by minimizing the following function:

$$\begin{aligned} F(\mathbf{H},t)=&\sum_{p_l\in\mathbf{P}(t)}\left\|\tilde{h}_{idx(l)}(t)-p_l(t)\right\|^2 \\ &+\alpha\sum_{k=0}^{l}\sum_{j=0}^{m}\sum_{i=0}^{n}\left\|P_{ijk}(t)-P_{ijk}(1)\right\|^2 \end{aligned} \qquad (4)$$

where the first term is the sum difference between each *l*-th vertex p_l in the reconstructed LV mesh $\mathbf{P}$ and its corresponding paired vertex $h_{idx(l)}$ in the heart model, and the second term is a regularization to maintain uniform distribution of control points P_{ijk}. For more realistic heart contraction, the motion of the other heart chambers for example the RV should be considered concurrently.

The dynamic heart model is re-encoded as a boundary enhanced cubic voxel representation to facilitate fast collision detection and response. The voxelization of the heart model describes a voxel type (heart, non-heart, heart-surface or non-heart surface), a normalized distance from the nearest heart surface, and an associated surface triangle index. Collision detection between the catheter and heart surface can be determined by retrieving the voxel information of the catheter nodes. If a catheter node is near to the heart surface, the moving average of the surface normal is computed from neighborhood of the indexed surface triangle and the distance of the node from surface is re-computed. A contact is detected if any catheter nodes belong to heart voxel type or if any node has zero or negative distance from the nearest heart surface.

Compared to a static heart model, a dynamic heart model introduces new challenges to simulate the interaction between catheter and heart surface [25]. We first simplify the dynamic interaction into quasi-static phases of interaction where either motion of the heart wall or the catheter is considered separately. The time interleaving of catheter and heart motion phases allows for realistic moving bodies simulation. In the catheter motion phase, the interaction remains the same as in the static heart model. In the heart motion phase, the initial contact type and position between the moving heart surface and the

stationary catheter is computed. From the discrete spatio-temporal voxel representation, the catheter nodes near to the heart surface are identified. If the nearest node belongs to the catheter tip region, then a stable contact is first formed. The surface triangles in the vicinity of the catheter tip are bi-linearly interpolated in the temporal domain according to the distance from surface. A search is executed in the interpolated surfaces to locate the triangle nearest the tip and the associated moving average distance is computed. Surface interpolation and nearest distance computation are repeated with the updated distance until the initial contact position is found.

On stable contact, the deformation of the catheter between the contact and the insertion is modeled by a two-step memory recursive shape deformation. An initial shape deformation is described by sum of weighted force displacements:

$$q_i^0(t) = q_i(t-1) + w_{a,i} f_{I,i}(t) + w_{b,i} f_{N,i}(t) \qquad (5)$$

where $f_{I,i}(t)$ is force displacement attributed to the shift in aortic orifice, $f_{N,i}(t)$ is the force displacement at catheter tip due to heart wall contraction. The weight distributions of the force displacements along the catheter length are given by $w_{a,i} = \left(\frac{N-i}{N-I}\right)^3$ and $w_{b,i} = 1 - \left(\frac{N-i}{N-I}\right)^3$. The final deformation is computed by minimizing the strains E on the catheter:

$$E = \beta \sum_{i=I}^{N} |\theta_i - \phi_i| / 2\pi \sum_{i=I}^{N-1} l_i + (1-\beta) \sum_{i=I}^{N-1} |\xi_i - l_i| / \sum_{i=I}^{N-1} l_i \qquad (6)$$

where ϕ_i and θ_i refer to the catheter curvatures, l_i and ξ_i refer to the catheter segment length before and after deformation, and β balances between the lateral and axial strains. In subsequent heart or catheter motion, the stability of the contact is assessed using

catheter strain and catheter-tissue angles. High strain and low angles result in an unstable contact, where the catheter deformation is simulated similar to catheter interaction with the static heart model.

3. Results and Discussion

3.1 Linear Local Shortening

The 3D motion of the LV is reconstructed from tMRI by solving the proposed deformation optimization function and we present the results for LV strain and torsion. Rather than the Lagrangian strain tensor derived from a volumetric model [10] or the circumferential strain from a latitude segment length change [18], the mechanical function of the LV and its local wall motion can be assessed by means of linear local shortening (LLS) [26]. LLS provides the diagnosis of the myocardial surface contractile function. The range of LLS when comparing end diastole and systole states and their indication of myocardial functionality is listed in Table 1.

Table 1: LLS range and contractile description

LLS Range	Contractile Description
LLS≥12%	normal
8%<LLS<12%:	mild impairment
4%<LLS<8%:	moderate impairment
0<LLS<4%:	severe impairment (hypokinesis or akinesis)
LLS≤0%	paradoxical increase (dyskinesis)

Denoting p_i as the *i*-th vertex of the reconstructed LV mesh and $d_{ij} = \|p_i - p_j\|$ as the Euclidean distance between the *i*-th and *j*-th vertices, we define the LLS of p_i at time t with respect to the initial frame at end diastole t_{ED} by:

$$lls(p_i, t) = \sum_{j \in N(i)} \alpha_{ij} (1 - d_{ij}(t) / d_{ij}(t_{ED})) \qquad (7)$$

where $N(i)$ is the neighborhood of the *i*-th vertex and α_{ij} is the radial basis weight defined as $\alpha_{ij} = e^{-k(d_{ij}-c)^2}$. We set $c = 8$, $k = 0.1$ when $d_{ij} < c$ and $k = 0.05$ when $d_{ij} \geq c$ heuristically. c affects the radial distance of influence while k controls the slope of the weight. In all results presented thereon, we use an initial frame captured after end diastole at $t = 3$ because the quality of preceding frames is poor. Fig. 4 shows the LLS profile of the reconstructed LV mesh with respect to time in frame and distance from apex. The data at *x* distance from apex refers to the averaging of the vertex data from a slice located at a normalized distance $[x - 0.1, x]$ from the apex. LLS increases rapidly from frame 3 near end diastole. It peaks during systole at frames 10-12 before decreasing quickly to zero at frame 17. Across the distance from apex to base, the LLS is higher near apical slices with a maximum of 0.2 at a normalized distance of 0.3 and then it gently decreases towards the base. The range of LLS and its general decrease along apex-base axis is consistent with the circumferential strain reported in [18]. Fig. 5 shows the LLS distribution on the reconstructed LV in time series and different views. The maximum LLS is observed from frame 9 to frame 12 near the apex region.

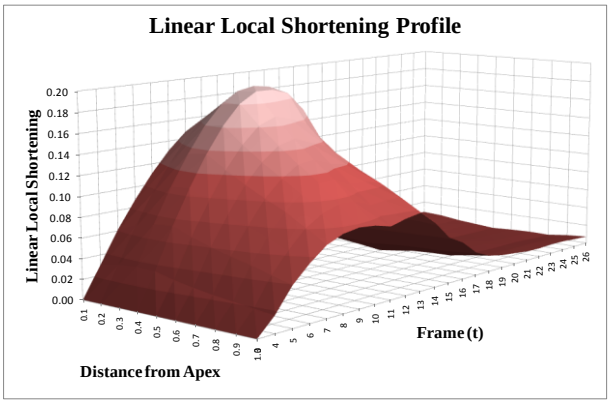

(a) Surface plot

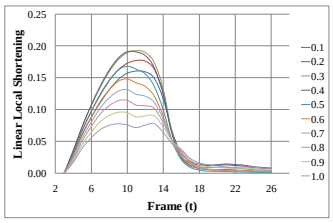

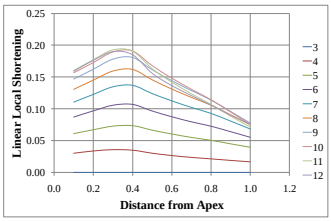

(b) Distance from apex series *(c) Frame series*

Fig. 4: LV linear local shortening profile.

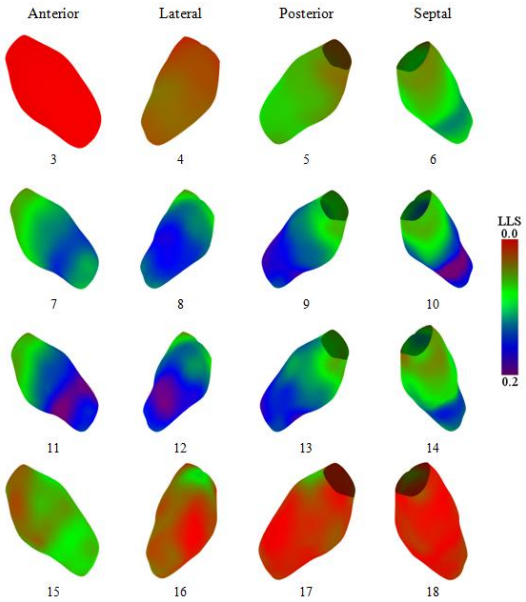

Fig. 5: Composite map of LLS on LV model with anterior, lateral, posterior, septal views for frames 3-18.

3.2 Axial Twist

The torsion of the LV is measured by the axial twist. Defining twist to be evaluated on the apex-to-base axis, we project each mesh vertex p_i to the apex-to-base axis at p_i'. The

twist angle is computed as the rotation angle of vector $p_i p_i'$ from t to t_{ED} with respect to the axis less the global axial rotation of the LV. A positive twist indicates a counter clockwise rotation directed from apex to base while a negative twist indicates clockwise rotation. The twist angles are further compensated by the alignment of the base-apex axis at end diastole. The first 1% of vertices on the apex-to-base axis is excluded due to large angle errors generated at apex. Fig. 6 shows the axial twist profile varying with time and slice. The profile shows that the slices near the apex (0.1-0.4) undergo counter clockwise rotation while the slices near the base (0.6-1.0) undergo clockwise rotation. This anti-rotation along the base-apex axis produces the axial twist with its center migrating from 0.57 towards the apex as ti me increases. From the timeline, the angle near the apex increases as the apical slices rotate counter clockwise up to a maximum at frame 10 during systole, then decreases as the apical slices rotate clockwise. On the other hand, the basal slices rotate clockwise to twist the LV during pre-systole and they rotate counter-clockwise to untwist the LV during post-systole. The frame series results are consistent with prior arts [9][12] while the surface plot is similar with meshless model described in [11]. The total twist angle deviation from base to apex is 10.3º and is smaller than 14º reported in [9] and between 10.3º outer wall and 20º inner wall figures in [12].

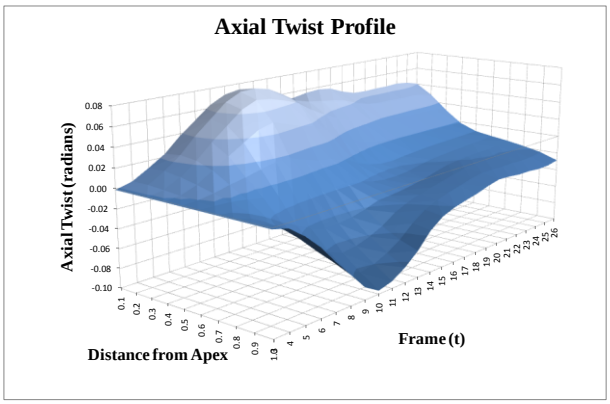

(a) Surface plot

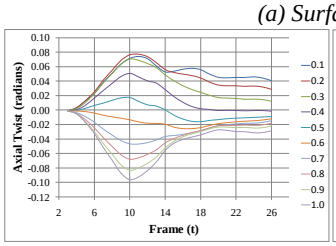

(b) Distance from apex series

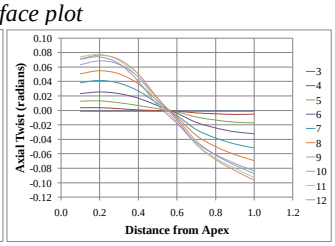

(c) Frame series

Fig. 6: LV axial twist profile.

3.3 Radial and Longitudinal Compression

To determine the global shape deformation, the radial and longitudinal compressions are measured. Fig. 7a shows the average radius profile for different slices and time. From the apex to the base, the radius increases gradually, peaks at distance 0.7, and then decreases. The average apical radius has a larger offset due to the exclusion of some apex vertices while the confidence of the basal radius is affected by the open LV mesh model. Denoting $r(t)$ as average radius of a slice with distance from the apex, we define the radial strain by:

$$\varepsilon_r(t) = r(t)/r(t_{ED}) - 1 \qquad (8)$$

From Fig. 7b and Fig. 7c, the radial compression increases and then decreases across the apex-base axis and the time axis. The largest radial compression is observed at mid ventricular slice of distance 0.4 and at systole frames 10-12. The expansion for upper

half of the LV from frame 17 to frame 26 is due to the initial frame being captured after end diastole. The maximum radial compression of 25% is between the outer wall radial strain of 15-20% in [9] and inner wall radial strain of 35% in [12]. The basal radial compression of 10% is similar to [9].

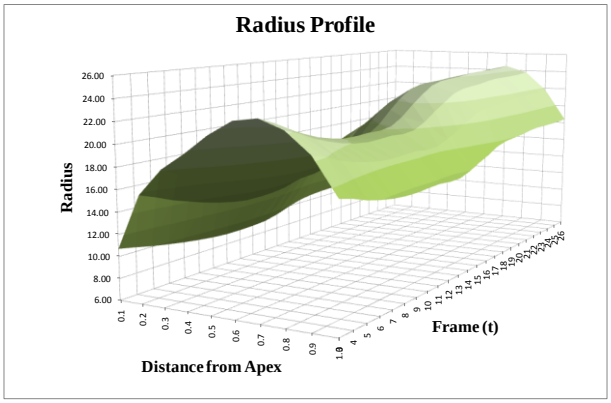

(a) Surface plot

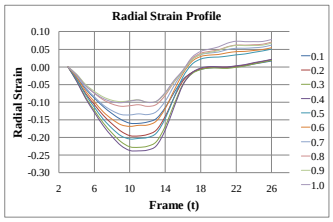

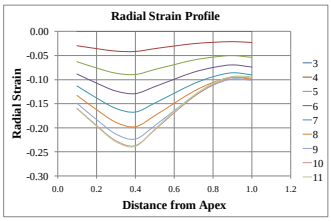

(b) Distance from apex series *(c) Frame series*

Fig. 7: LV radius and associated radial strain profile.

From Fig. 8a, we observe a downward displacement of vertices along base-apex axis during pre-systole and an upward displacement during post-systole and the crossing of the zero line at frame 14. This displacement along base-apex is computed by tracking the center of base-apex axis and projecting it to the axis at end diastole. Let the length of the base-apex axis at time t be $l(t)$, the longitudinal strain is:

$$\varepsilon_l(t) = l(t)/l(t_{ED}) - 1 \qquad (9)$$

The profile for longitudinal strain in Fig. 8b shows a similar trend along the time axis as radial strain. There is an increase in longitudinal compression during pre-systole and a decrease during post-systole with an expansion from frame 18. The maximum range of

longitudinal compression of 16% is below the 40% reported in [11] but greater than 12% in [9].

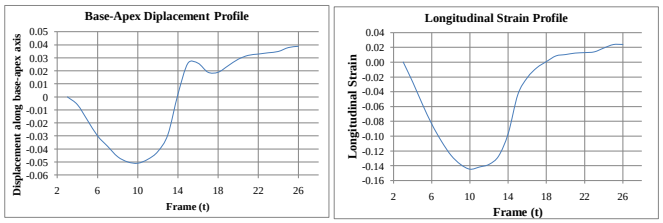

(a) *(b)*

Fig. 8: LV base-apex displacement and associated longitudinal strain profile.

The four major phases of ventricular motion [27] are described herein with comparison to observations from the LV motion reconstruction. In the isovolumic contraction phase, global counter-clockwise twisting occurs, resulting in bidirectional transient lengthening and downward displacement of the LV. The initial rotation and lengthening is missed due to the delay of the initial frame. In preparation for the ejection phase, contraction down the descending segment occurs with clockwise rotation at the base and counter-clockwise rotation at the apex and results in longitudinal shortening. Both the twisting and shortening are observed in Fig. 6b and Fig. 8b from frame 3 to frame 11. This is followed by the isovolumic relaxation phase, where contraction up the ascending segment occurs with untwisting of apex, resulting in brisk upward motion of base and lengthening. The untwisting is seen in Fig. 6b with upward displacement and lengthening in Fig. 8 in frames 12-18. There is subsequent widening of basal area, eventually transiting to diastolic filling phase, where rapid clockwise untwisting and widening occurs with rapid filling of ventricle. The basal widening is observed in Fig. 7b near frames 17-19.

3.4 Reconstructed LV and Catheter-Heart Interaction

Fig. 9 shows an exemplary intra-cardiac intervention where the catheter is inserted into the left ventricle via the aortic orifice and touches the inferior lateral wall near the apex. The interaction of the catheter with the dynamic heart model is simulated using the reconstructed LV model. As the heart contracts, the contact of the catheter tip remains while the catheter is deformed within the heart lumen. However, there is more room for improvement in the FFD technique used to transfer the deformation of the LV to the heart model and to integrate motions from different heart chambers.

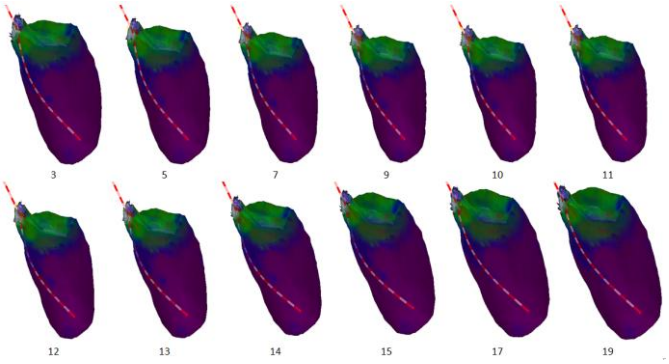

Fig. 9: Simulated interaction of catheter with patient specific heart model for frames 3-19.

4. Conclusion

The 3D motion of the LV is reconstructed from tMRI scans. A differential surface model is proposed to track spatial-temporal deformations. The proposed model minimizes the sum differences of the Laplacian surface and the sum differences of projected and tracked planar displacements. In this way, the deformation is optimized between the apparent motions from orthogonal planes while maintaining the surface curvature of the model. The spatio-temporal tracking produces strains and axial twists from the reconstructed LV

that are consistent with literature and yet offers a lighter complexity than 4D B-Splines and FEM models. With the reconstructed 3D motion of LV, we integrate patient specific motion data into the heart model of the VR simulator.

ACKNOWLEDGMENT

The authors like to thank Mr Julian Gan for his professional help on the cardiac tMRI scan. This work is partially supported by the MOE AcRF Tier 1 Grant of Singapore (T1-001-017).

REFERENCES

[1] D. Wei, "Whole-heart modeling: Progress, principles and applications", *Progress in Biophysics and Molecular Biology*, vol. 67, no. 1, pp.17-66, 1997.

[2] C.M. Ingrassia, T.P. Usyk, R.C.P. Kerckhoffs, A.D. McCulloch, K.D. Costa, J.W. Holmes, "Model-based development of four-dimensional wall motion measures', *Computer Methods in Applied Mechanics and Engineering*, vol. 196, no. 31, pp. 3061–3069, 2007.

[3] L. Xia, M. Huo, Q. Wei, F. Liu, S. Crozier, "Analysis of cardiac ventricular wall motion based on a three-dimensional electromechanical biventricular model", *Physics in Medicine and Biology*, vol. 50, no. 8, pp.1901–1917, 2005.

[4] M. Sermesant, Y. Coudiere, H. Delingette, N. Ayache, J. Sainte-Marie, D. Chapelle, F. Clement, M. Sorine, "Progress towards model-based estimation of the cardiac

electromechanical activity from ECG signals and 4D images", *ESAIM proceedings*, vol. 12, pp. 153-162, 2002.

[5] T. Arts, W.C. Hunter, A. Douglas, A.M.M. Muijtjens, R.S. Reneman, "Description of the deformation of the left ventricle by a kinematic model", *Journal of Biomechanics*, vol. 25, no. 10, pp. 1119–1127, 1992.

[6] E. Waks, J.L. Prince, A.S. Douglas, "Cardiac motion simulator for tagged MRI", *Proceedings of Mathematical Methods in Biomedical Image Analysis*, pp. 182–191, 1996.

[7] L.K. Waldman, J.J. Allen, R.S. Pavelec, A.D. McCulloch. "Distributed mechanics of the canine right ventricle: effects of varying preload", *Journal of Biomechanics*, vol. 29, no. 3, pp. 373–381, 1996.

[8] W.G. O'Dell, C.C. Moore, W.C. Hunter, E.A. Zerhouni, E.R. McVeigh, "Three-dimensional myocardial deformations: Calculation with displacement field fitting to tagged MR images", *Cardiac Radiology*, vol. 195, no. 3, pp. 829-835, 1995.

[9] J. Park, D. Metaxas, L. Axel, "Analysis of left ventricular wall motion based on volumetric deformable models and MRI-SPAMM", *Medical Image Analysis*, vol. 1, no. 1, pp. 53-71, 1996.

[10] I. Haber, D.N. Metaxas, L. Axel, "Three-dimensional motion reconstruction and analysis of the right ventricle using tagged MRI", *Medical Image Analysis*, vol. 4, no. 4, pp. 335-355, 2000.

[11] X. Wang, D. Metaxas, T. Chen, L. Axel, "Meshless deformable models for LV motion analysis", *Proceedings of IEEE Conference on Computer Vision and Pattern Recognition*, art. 4587565, 2008.

[12] G. Luo, P.A. Heng, “LV shape and motion: B-Spline-based deformable model and sequential motion decomposition” *IEEE Trans. Information Technology in Biomedicine*, vol. 9, no. 3, pp. 430-446, 2005.

[13] C. Ozturk, E.R. McVeigh, “Four dimensional B-Spline based motion analysis of tagged cardiac MR images”, *Proceedings of SPIE*, no. 3660, pp. 46-56, 1999.

[14] J. Huang, D. Abendschoen, V.G. Davila-Roman, A.A. Amini, “Spatio-temporal tracking of myocardial deformations with a 4-D deformation with a 4-D B-Spline model from tagged MRI”, *IEEE Trans. Medical Imaging*, vol. 18, no. 10, pp. 957-972, 1999.

[15] J. Li, T.S. Denney TS, ‘Left ventricular motion reconstruction with a prolate spheroidal B-Spline model’, *Physics in Medicine and Biology*, vol. 51, no. 3, pp. 517-537, 2006.

[16] N.J. Tustison, D. Abendschein, A.A. Amini, “Biventricular myocardial kinematics based on tagged MRI from anatomical NURBS models”, *Proceedings of IEEE Conference on Computer Vision and Pattern Recognition*, vol. 2, pp. II514-II519, 2004.

[17] W.S. Kerwin, J.L. Prince, “Cardiac material markers from tagged MR images”, *Medical Image Analysis*, vol. 2, no. 4, pp. 339-353, 1998.

[18] L. Pan, J.L. Prince, J.A.C. Lima, N.F. Osman, “Fast tracking of cardiac motion using 3D HARP”, *IEEE Trans. Biomedical Engineering*, vol. 52, no. 8, pp. 1425-1435, 2005.

[19] S. Sampath, J.L. Prince, “Automatic 3D tracking of cardiac material markers using slice-following and harmonic-phase MRI”, *Magnetic Resonance Imaging*, vol. 25, no. 2, pp. 197-208, 2007.

[20] P. Chiang, J. Zheng, K.H. Mak, N.M. Thalmann, Y. Cai, “Progressive surface reconstruction for heart mapping procedure”, *Computer Aided Design*, vol. 44, no. 4, pp. 289-299, 2012.

[21] H.R. Pakdel, F. Samavati, “Incremental adaptive loop subdivision’, *Lecture Notes in Computer Science*, vol. 3045, pp. 237-246, 2004.

[22] M. Meyer, M. Desbrun, P. Schröder, A. Barr, “Discrete differential geometry operators for triangulated 2-manifolds”, *Proceedings of VisMath*, 2002.

[23] M. Alexa, “Differential coordinates for local mesh morphing and deformation”, *The Visual Computer*, vol. 19, no. 2, pp. 105-114, 2003.

[24] O. Sorkine, M. Alexa, “As-rigid-as-possible surface modeling”, *Symposium on Geometry Processing (Eurographics)*, pp. 109-116, 2007.

[25] P. Chiang, Y. Cai, K.H. Mak, M.S. Ei, C.K. Chui, J. Zheng. “A geometric approach to the modeling of the catheter–heart interaction for VR simulation of intra-cardiac intervention”, Computer & Graphics, vol. 35, no. 5, pp. 1013-1022, 2011.

[26] R. Kornowski, M.K. Hong, L. Gepstein, S. Goldstein, S. Ellahham, S.A. Ben-Haim, M.B. Leon. “Preliminary animal and clinical experiences using an electromechanical endocardial mapping procedure to distinguish infarcted from healthy myocardium”, *Circulation*, vol. 98, no. 11, pp. 1116-1124, 1998.

[27] G.D. Buckberg, J.L.E. Hoffman, A. Mahajan, S. Saleh, C. Coghlan, "Cardiac Mechanics Revisited: The relationship of cardiac architecture to ventricular function", *Circulation*, vol. 118, no. 24, pp. 2571-2587, 2008.

[28]P. Chiang, J. Zheng, Y. Yu, K. Mak, C. Chui, Y. Cai (2013), A VR Simulator for Intracardiac Intervention: Concept, Design and Implementation, **IEEE Computer Graphics and Applications** 33(1): 44-57.

[29]P. Chiang, Y. Cai, K. Mak, C. Chui, J. Zheng (2010), A geometric approach to the modeling of the catheter heart interaction for VR simulation of intra-cardiac intervention, **Computers & Graphics** 35(5): 1013-1022

[30]P. Chiang, J. Zheng, K. Mak, N. Thalmann, Y. Cai (2011), Progressive Surface Reconstruction for Heart Mapping Procedure, **Computer-aided Design** 44 (2012) 289–299.

[31]P. Chiang, Y. Cai, K. Mak, J. Zheng (2013), A B-Spline Approach to Phase Unwrapping in Tagged Cardiac MRI for Motion Tracking, **Magnetic Resonance in Medicine**, Online first publication available.